Multisystem Modeling and Optimization of Solar Sintering System

C. Morris*, D. Debeau*, A. Dressler *, C. C. Seepersad *

*Department of Mechanical Engineering, The University of Texas at Austin

Abstract

In developing countries, the production of building materials such as tile and brick, require large amounts of non-renewable energy and/or time to produce. Previous work has shown that solar sintering machines are capable of producing ceramic parts in a viable amount of time using only solar energy. The systems focus sunlight on a bed of sand where the intensity is sufficient for sintering. Then by moving the sand bed, parts of complex geometry are formed.

This study aims to identify optimal operating parameters for the solar sintering system by solving a multi-objective, multisystem model. The subsystems considered are the dynamics of the sand bed, optics of focusing sunlight, and heating of the sand bed. To reduce the computational expense, a Kriging surrogate model was employed to model the heating of the sand bed. Finally by performing a tradeoff analysis of production time and part quality, candidate operating parameters were identified.

Introduction

Solar sintering stations (SSS) can produce tiles, and even structures of arbitrary shape, by focusing sunlight via a Fresnel lens to sinter sand on a motorized bed [1]. These systems are of particular interest because they can be powered entirely by the sun and use sand, a readily available material, to manufacture useful products like tiles or bowls. Due to the resources needed to run the systems, they can be readily employed in regions that lack access to electricity but have abundant sunlight and sand.

While multiple systems have been developed and tested, there is a lack of information on their development in the literature. Numerous papers have explored the sintering of sands and ceramics using selective laser sintering but the effects of a Fresnel lens as the heat source is largely unexplored [2] [3]. The thesis of Rietema provides an initial analysis of the subsystems that constitute a solar sintering system, but fails to consolidate each subsystem into a comprehensive system model [1]. Therefore, there is a need for a full system model which will be a stepping stone in the implementation of SSS in developing countries

To make solar sintering a viable manufacturing option for tile production, various objectives must be accomplished. These objectives are, minimizing the power required to operate the system, maximizing the quality of the tiles, and minimizing the time required to produce a tile. Due to the opposing nature of these objectives, identification of a single optimal design is not possible. Rather a Pareto set of performance can be identified and candidate operating parameters can be back-propagated from the Pareto set. Then, suitable operating parameters can be selected based on user need. In order to determine the Pareto set and candidate designs, the

entire system must be decomposed into various subsystems, that model each component of the system.

Figure 1 illustrates the subsystem hierarchy and organization where the four subsystems- Fresnel Lens, path planning, mechatronics, and heat transfer model -are carefully coordinated to model performance which is then optimized. More details of each subsystem will be provided in the following paragraphs, but a general overview of the system is provided here for clarity.

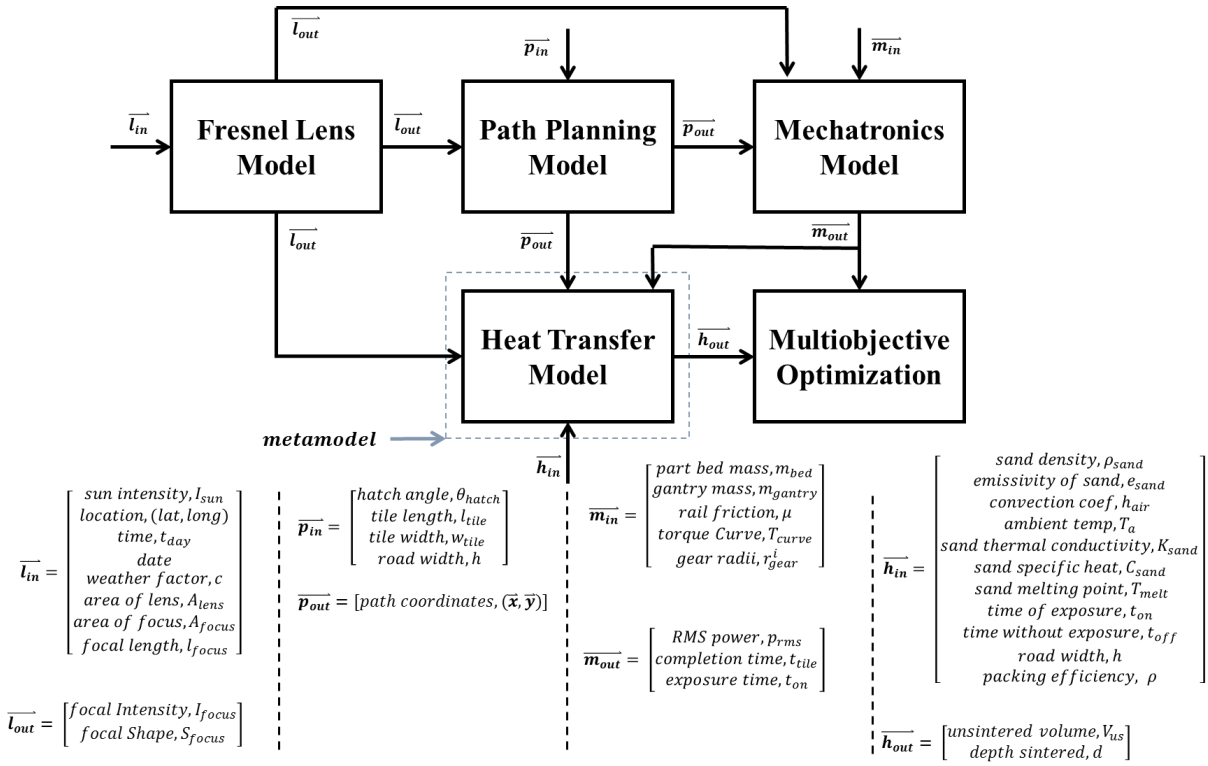

Figure 1. Flowchart of subsystems as well as design and performance variables

The first subsystem of the model is the Fresnel Lens Model which uses the geometry of the lens, weather conditions, and location to output the characteristics of a focused beam, which are its shape and intensity. The output of the Fresnel Lens Model then becomes the input to three different subsystems: Path Planning, Mechatronics, and Heat Transfer. The Path Planning Model uses the geometry of the beam and a user specified road width to determine the coordinates the bed must travel to on each pass when forming the tile. These path coordinates are introduced to the Mechatronics Model where a dynamic analysis coupled with a motion planning strategy yield the total time per pass, RMS motor power, and time of exposure for a point on the sand bed. The outputs of all the subsystems, (Fresnel Lens, Path Planning, and Mechatronics), become inputs to the Heat Transfer Model of the sand bed where the non-sintered region as well as the depth sintered will be determined. Due to the large number of inputs to the Heat Transfer Model and computational expense of using finite element analysis to determine the temperature of the sand bed, a Kriging metamodel is trained from previously evaluated design parameters to expedite the optimization process. The optimization process is encompassed in the Multiobjective Optimization Model, which receives the outputs of the Mechatronics and Heat Transfer Models in order to determine the set of solutions that lead to the desired performance. This desired

performance is a high quality tile that requires minimal energy to produce in a short amount of time.

In order to obtain the set of designs that will lead to the desired tiles, each of the subsystems previously discussed must be carefully considered. The following section presents detailed descriptions of the work completed and proposed to develop each system.

Fresnel Lens Model

The first portion of the simulation models the optics of the Fresnel lens to output the light intensity profile on the sand bed. After inputting date, time, location, and weather conditions, the model outputs the focus shape and intensity distribution. These outputs are used to determine the sand bed path and the heat transfer into the sand.

Before starting the sintering process, the angle of the lens needs to be adjusted to be perpendicular to the sunrays. The angle of the sunlight depends on the date, time, and location on earth (latitude and longitude). The angle of sun above the horizon is based on calculations from the Earth Systems Research Laboratory (ESRL), part of the National Oceanic and Atmospheric Administration [4].

The focus shape depends on the location of the sun in the sky since the angle will skew the shape from a circle to an ellipse as demonstrated in Figure 2. Assuming that radius of light is constant for a small window at the focal length, the shape of focused light on the sand bed can be calculated from the angle of the sun above the horizon and the focal radius when the sun is directly overhead.

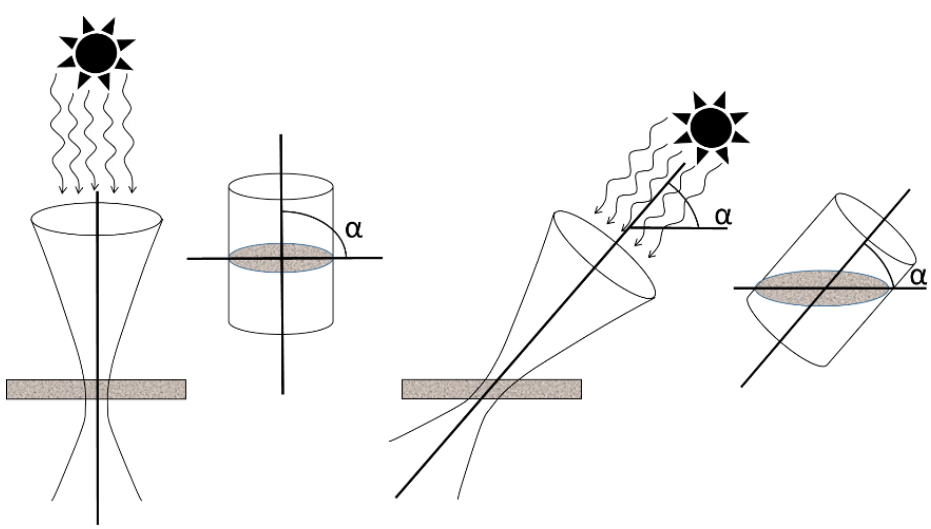

Figure 2. Depiction of how the angle of the sun impacts focal shape

The focal shape's minor radius is constant and equivalent to the focal radius with direct sunlight, r_{focal}, and the major radius**, a**s shown in Equation 1**,** where α is the angle of sunlight above the horizon. As a check, direct sunlight ($\alpha=90°$) yields a major radius equal to the focal radius resulting in a circular focal shape.

$$r_{major} = r_{focal}\left(cos(90° - \alpha) + \frac{sin^2(90°-\alpha)}{cos(90°-\alpha)}\right) \quad (1)$$

The manufacturer's lens specifications were "beam size max power--.4 inch (2.7" outer area 900 F)" [5]. Since the actual focal size was unclear based on these specifications, a simple experiment was conducted to determine the focal diameter. The lens was placed above the ground at the appropriate focal length while a LED flood lamp was held directly above the lens. The diameter of the focused light was measured at 10 mm.

The solar intensity experienced on earth depends on location, time of year, and the weather. First, the intensity at the edge of the atmosphere perpendicular to the sunrays, I_a, must be calculated as shown in Equation 2. Next, the intensity at the edge of the atmosphere parallel to the chosen location on earth, I_{ah}, needs to be calculated as shown in Equation 3. In the intensity calculations, I_{sc} is the solar constant, n is the day of the year, and α is the angle of the sun above the horizon.

$$I_a = I_{sc}[1 + 0.34\, cos(2\pi n/365.25)] \quad (2)$$

$$I_{ah} = I_a \cos \alpha \quad (3)$$

Finally, the intensity on the surface, I_{sun}, can be calculated based on what happens from the edge of the atmosphere to surface as shown in Figure 3. Part of the intensity is lost, due to scattering and diffuse reflection in the atmosphere while the rest of the losses depend on the weather. On a clear day, some of the intensity is absorbed into air particles. When the light passes through clouds, there are losses due to both reflection, and absorption in the clouds.

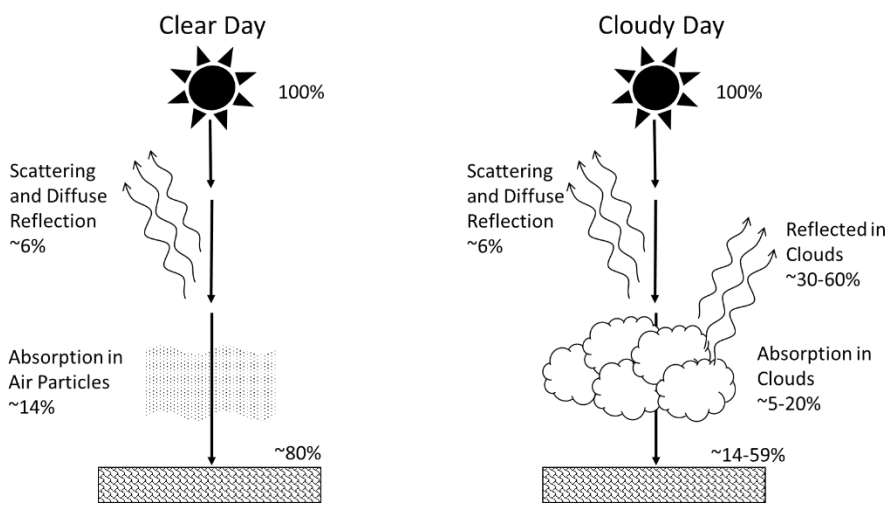

Figure 3. Intensity losses through the atmosphere dependent on weather [6]

Since cloudy days have a range of losses, the model requires a weather parameter to discount the intensity based on how many clouds are in the sky.

It has been well documented that the intensity at focal point of a Fresnel lens, commonly referred to as a solar concentrator, is non-uniform and follows a Gaussian distribution whose equation is given by Equation 4 [7] [8], where I is the intensity, r is the radius from the center of

the beam, ω_0 is the waist radius, and I_0 is the nominal intensity. It should be noted that the beam described here is for a lens that is parallel to the sand and has a circular shape. A more complicated focal point with an elliptical shape is used in the current model but the derivation for a circular beam is shown for simplicity. The methodology shown can be extended to elliptical geometries.

$$I(r) = I_0 e^{-\frac{2r^2}{\omega_0}} \tag{4}$$

The literature contains numerous methods for determining I_0 and ω_0 but all of these rely on knowing properties of the Fresnel lens [9] [10]. Unfortunately, the Fresnel lens available for the SSS lacks a technical sheet with information about the focal point and intensity. Therefore, rough calculations and some simple assumptions were made to characterize the beam. The main assumption was that at a diameter of 10mm the intensity will be 1/15 the intensity at a diameter of 1mm at the focal point. With this relation, ω_0 can be determined via Equation 5 where r_1 is the inner, high intensity radius and where r_2 is the outer, low intensity radius.

$$\omega_0 = \sqrt{-\frac{2\left(r_1^2+r_2^2\right)}{ln(15)}} \tag{5}$$

Finally, the nominal intensity can be determined through an energy balance. The power imparted to the lens must be equal to the power of the focal point. Equation 6 gives the relationship that yields I_0.

$$I_0 = \frac{I_{sun} A_{lens}}{\int\int e^{-\frac{2r^2}{\omega_0}} dA} \tag{6}$$

With the Gaussian beam determined it can now become input to the Path Planning, Mechatronics, and Heat Transfer Models.

Path Planning Model

The Path Planning Model determines what path the sand bed must take to sinter the tile. It receives as input the hatch angle, θ_{hatch}, tile length, l_{tile}, tile width, w_{tile}, and road width, h. The model also must compensate for the beam radius, r_{beam} so that the part can be accurately produced. The Path Planning Model begins by outlining the shape of the tile then hatching the internal pattern where the distance separating each hatch is determined by the road width and beam radius. The output of the model are the vertices, $(x_{\mathrm{i}},\ y_{\mathrm{i}})$, that when connected in sequence form the path the sand bed will take. Figure 4 shows the path and vertices of a representative tile.

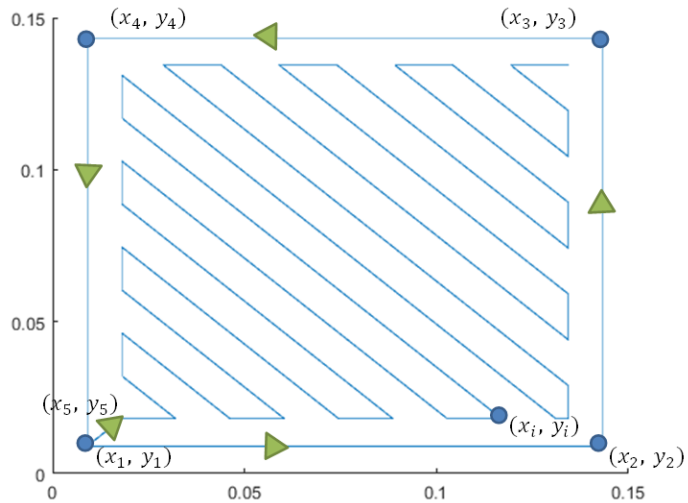

Figure 4. Illustration of Path Planning Model output

Mechatronics Model

The goal of Mechatronics Model is to determine the RMS motor power, p_{RMS}, completion time, t_{tile}, and the exposure time of a point, t_{on} when the sand bed is in motion. In order to determine these values, the model requires the spot radius, path coordinates, characteristic torque curve, T_{curve}, and number of passes, n_{cycles}. It also requires the mechanical properties of the system which are the mass of the sand bed, m_{bed}, the mass of the sand bed gantry, m_{gantry}, friction of the gantry, μ, and the radii of the driving gears, r_{gear}. Through a simple Newtonian analysis, Equations 7 and 8 show the torque, T_x and T_y, required to accelerate the sand bed in the x and y directions, a_x and a_y.

$$T_x = r_{gear}(m_{bed} + m_{gantry})(a_x + \mu g) \tag{7}$$

$$T_y = r_{gear} m_{bed}(a_y + \mu g) \tag{8}$$

As Equations 7 and 8 show, the acceleration must be prescribed in order to determine the torque. The acceleration in the x and y directions are determined by solving a series of univariate boundary value problems where the boundary positions are the adjacent vertices of the path coordinate matrix, $(x_{\mathrm{i}}, y_{\mathrm{i}})$ and $(x_{\mathrm{i+1}}, y_{\mathrm{i+1}})$, the boundary velocities are instantaneously zero, the accelerations are instantaneously zero, and the jerks are continuous across line segments. This is done to ensure the electrical load on the motors is continuous and non-impulsive.

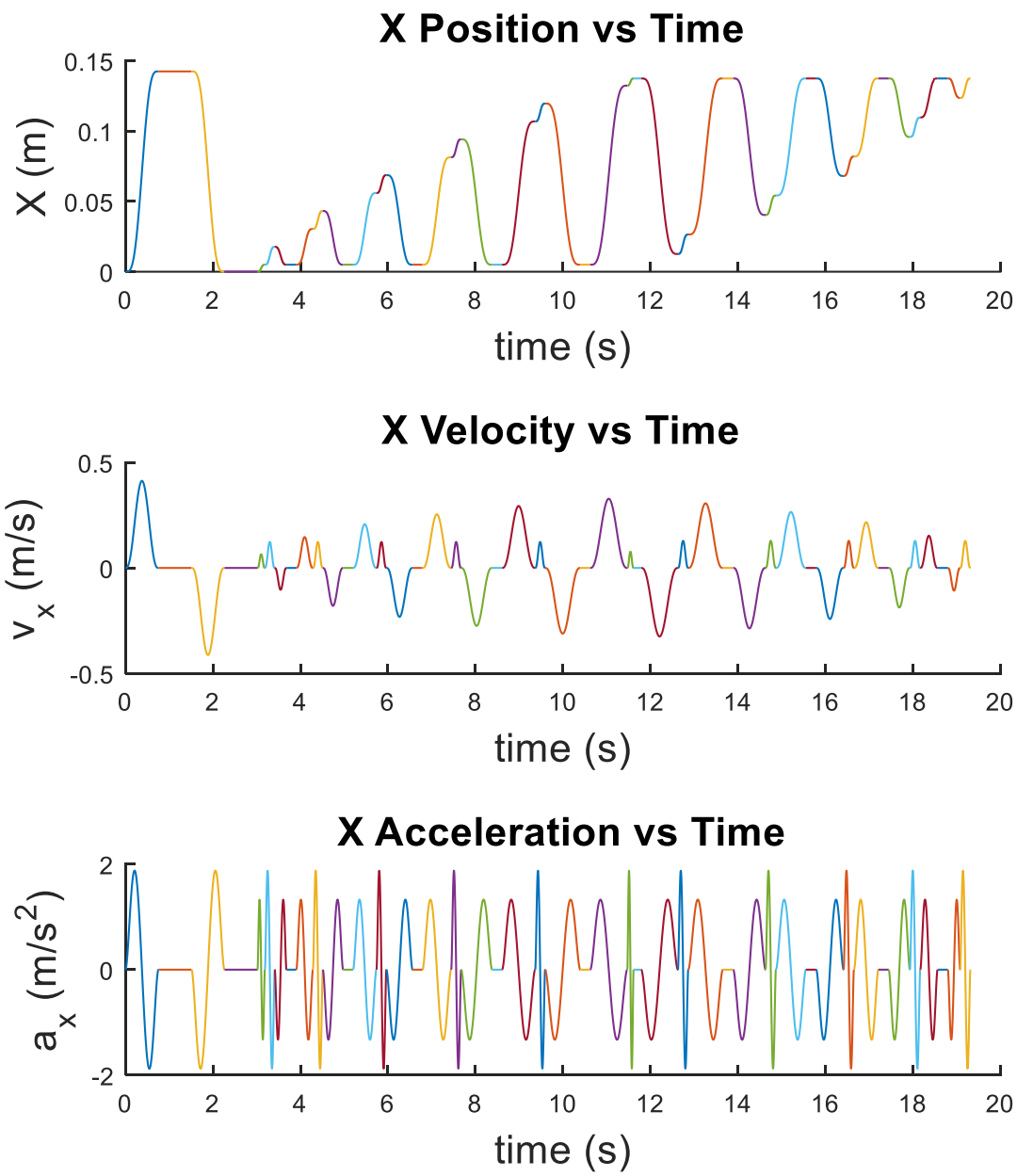

Figure 5. Example output of the motion planning model. The position is shown on the top, velocity is in the middle, and acceleration is on the bottom.

In Figure 5. Example output of the motion planning model. The position is shown on the top, velocity is in the middle, and acceleration is on the bottom., each line color is associated with a different line segment of the motion plan. It can be seen that the velocities and accelerations at the junctions are zero as prescribed. Also the graph of the x position clearly matches the path needed to make the tile. The tracing of the perimeter is followed by the hatching pattern where the line segments grow then shrink symmetrically. From these graphs, there should be a smooth electrical input to the motor which will likely improve its longevity.

Another constraint imposed on the motion is the time it takes to traverse a line segment is a function of the length of the line segment itself. Equation 9 provides the relationship between the time taken to traverse a line segment, t_{seg} and the length of the line segment, l_{seg}. In Equation 9, γ and κ are tuning parameters that vary the impact of a line segments length on the time required to traverse it.

$$t_{seg} = \kappa l_{seg}^{\gamma} \tag{9}$$

Through this parameterization the average velocity across a line segment, v_{seg} can be specified by Equation 10. The average velocity can be tuned by varying the value of γ and κ which will be required to ensure the motion plan is within the constraints imposed by the motor torque curve. This constraint as well as others will be discussed later.

$$\bar{v}_{seg} = \frac{l_{seg}^{1-\gamma}}{\kappa} \tag{10}$$

With the torque requirements and velocity calculable, the exposure time of a point on the sand bed, t_{on} and total sintering time, t_{tile} can be determined by Equation 11 and Equation 12, respectively, where n_{seg} is the total number of line segments.

$$t_{on} = \frac{r_2}{v_{seg}} \tag{11}$$

$$t_{tile} = \sum_{i=1}^{n_{seg}} t^{i}{}_{seg} \tag{12}$$

Also the power can be determined by multiplying the torque by the angular velocity of the motor allowing the RMS power to be easily determined. Figure 6 shows a representative power curve for both motors that control motion in the x and y directions independently.

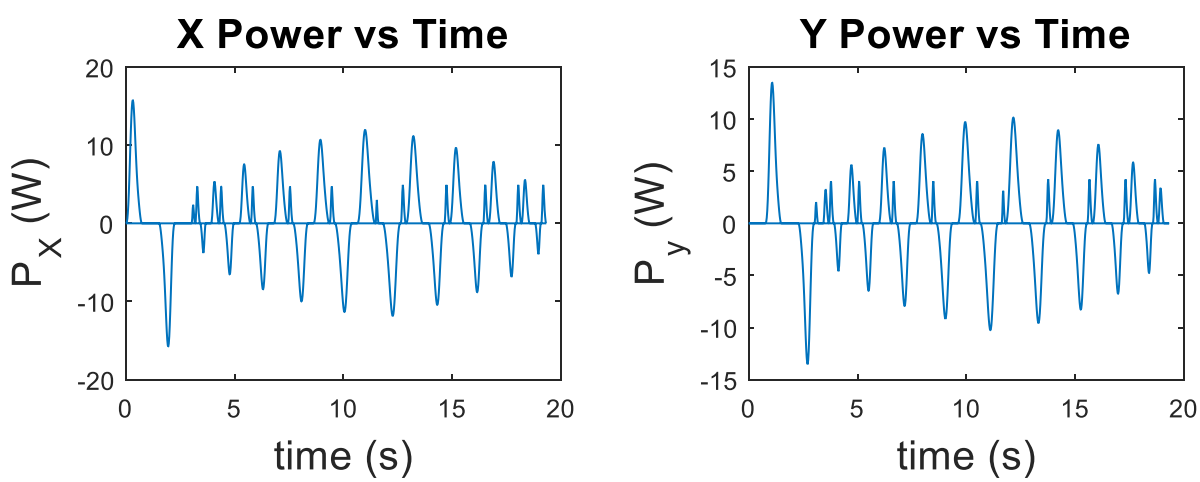

Figure 6. Power requirements of motor in the x and y directions

With the mechatronics system completely developed and the time of exposure determined, the heat transfer model can be discussed.

Heat Transfer Model

The heat transfer model is made in Abaqus, a graphical Finite Element Analysis (FEA) package. Abaqus has the ability to be programmed using python script, which allows the analyst to develop simulation models from configuration files and functions written in python. The end result of the programming is a library of functions, and a single configuration file, corresponding to a specific test. This method provides a convenient way for the analyst to log their tests, and allows the analyst to make quick changes and re-run simulations.

The heat transfer model begins with a simple block with the material properties of sand. The thermodynamic properties of sand were obtained from a heat transfer textbook [11]. On the forward facing surface of the block, an ellipse is cut, allowing a surface heat flux load to be applied to it. This load is varied across the ellipse using a Gaussian distribution, with parameters output from the lens model, see Figure 7.

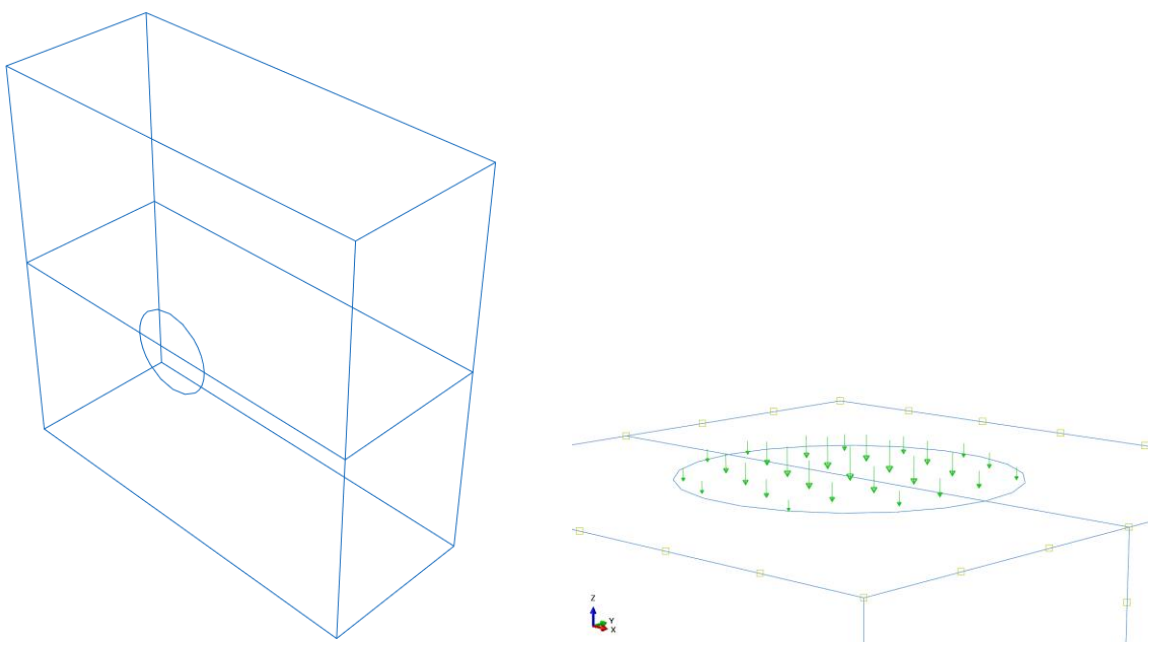

Figure 7. Material Block (left), and Gaussian Distribution of Heat Flux (right)

For the boundary conditions, all of the surfaces except for the load surface, are kept at a constant 300 K. This is to provide an accurate representation of the conditions present on the build platform. Care must be taken to insure that the block is large enough to prevent these surfaces from acting as heat sinks. This is monitored using a reaction heat flux output from Abaqus. If the magnitude of the reaction heat flux is too high, then the 300 K surfaces are too close to the heat flux load, and the block must be made larger. It is beneficial to have the block small however, as every element increases analysis time.

For an accurate analysis it was crucial to include natural convection and radiation interactions on the load surface. Both were applied, using an ambient temperature of 300 K. Through simulation, it became evident that the heat lost through radiation was orders of magnitude higher than the heat lost through convection. Further, due to the nonlinearity of the radiation equation, the net heat flux on the load surface rose quickly on the application of the

load, and then fell as the sintered area rose in temperature. This dependency on radiation is due to the high emissivity of the sand.

In order to verify the model that the model was working as intended, the approximate node temperature at the center of the load surface was calculated. This was done by taking an energy balance, Equation 13, and then using Matlab to compute the temperature. The intensity of the beam at the node is given by the lens model, and the total flux at the node is output by Abaqus.

$$I_{focus} - q_{convection} - q_{radiation} = q_{totalFlux} \tag{13}$$

$$q_{convection} = h_{air}(T - T_{ambient}), \;\; q_{radiation} = e_{sand}\sigma(T^4 - T_{ambient}^4)$$

The equation is then a 4th order polynomial:

$$(-2.83 * 10^{-8})T^4 - 2T \; + (3.62 * 10^7) = -2.75 * 10^6 \tag{14}$$

Using the solve function in Matlab yields a positive real value of 6086 K for node temperature, T in Equation 14. This is very close to the actual node temperature of 5732 K, which is output by Abaqus.

To confirm that the model was conducting heat correctly, the temperature of the node directly below the center node was calculated using Equation 15.

$$q_{totalFlux} = \frac{k_{sand}(T - T_{centerNode})}{L} \tag{15}$$

This yielded a temperature of 643 K, very close to the value output by Abaqus of 584 K. While the model is three dimensional, the close proximity of the nodes (0.5 mm), allows for the one dimensional heat conduction equation to be used.

Originally, the program took into account multiple passes of the light beam. Through experimentation this proved to not have an effect on the sintered profile. The amount of time taken between passes allowed the sand to cool significantly, which prevented subsequent passes from increasing the sintered depth. The model was then simplified, by keeping the number of passes at one, and not modeling the cool down of the sand between passes.

The block is cut in half with a partition to allow the mesh function in Abaqus to orient the elements so that the center nodes will align with the cut face, see Figure 7. The temperature of the nodes on the cut face are put through a function which determines the sintered depth and profile. This is output to a text file, allowing a Matlab function to determine the sintered volume. Due to the convex geometry of the sintered region, there must be some region that is not sintered so in order maximize the part quality, the volume of the region that is not sintered should be minimized. The volume of this region is a simple calculation that can be determined by the sintered profile, road width, *h*, and the path coordinates. By calculating the length of the segments between hatches and the vacant area between two sintered profiles separated by a distance that corresponds to the road width, the total volume of the non-sintered region can be determined. Figure 8 illustrates the area between two sintering profiles and the length of the segments between hatches.

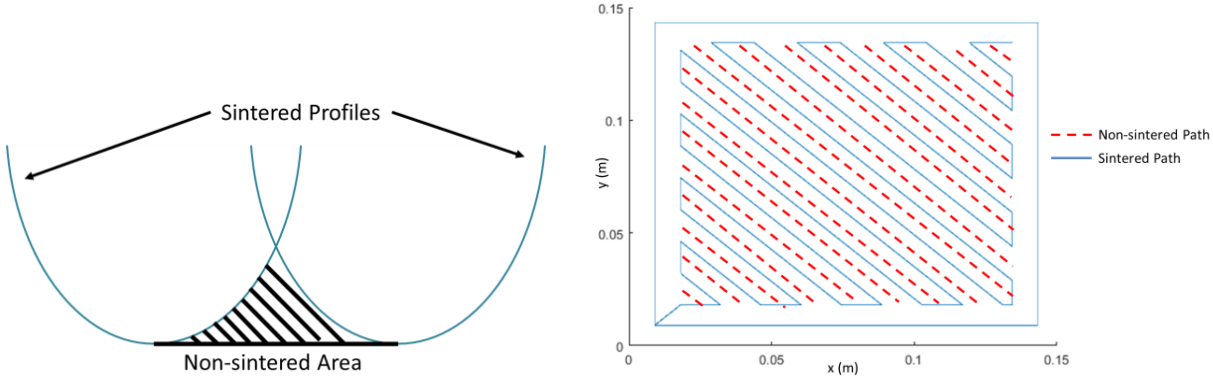

Figure 8. Determination of non-sintered area (left) and extruded length of non-sintered area (right)

The Heat Transfer Model receives inputs from each of the other subsystems which leads to a large number of design variables. Simulation of a single instantiation of the design variables is also computationally expensive to complete. As a result, brute force evaluation of the entire design space would take years for the Heat Transfer Model. Therefore, a Gaussian Kriging metamodel was used to alleviate the computational expense of the FEM simulation.

Metamodel

The Gaussian Kriging metamodel receives the light intensity, angle of lens, and time of exposure, as inputs and outputs the expected sintered profile which is a set of 21 xz −coordinates. In order to obtain the sintered profile, 42 different Kriging metamodels were trained to predict each component of the sintered profile coordinates. The training points were generated by a Halton sequence of 100 points where the design variables are the light intensity, angle of lens, and time of exposure. To determine the accuracy of each metamodel, the Absolute Average Error (AAE) value was determined for each model comprised of test data from the next 20 points in the Halton sequence. Figure 9 shows plots of the AAE for the x and z coordinates, respectively, of each model.

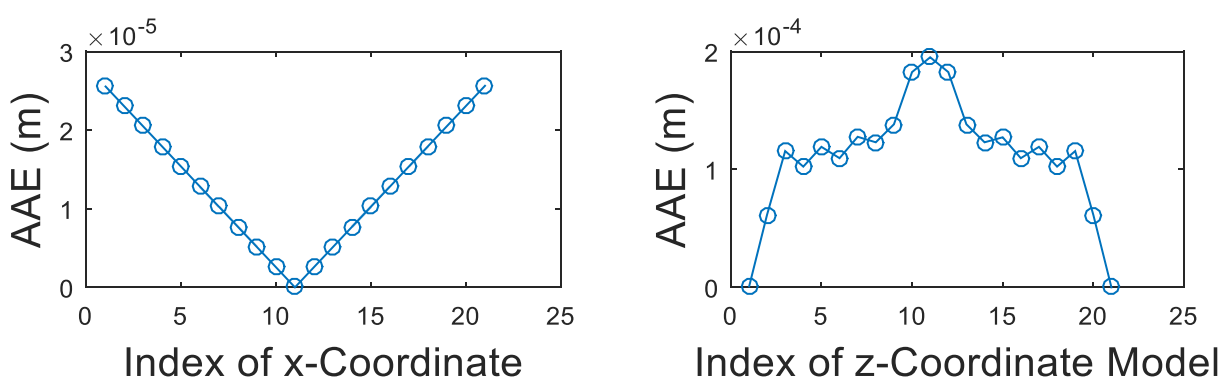

Figure 9. Average absolute error of each index for the coordinates of the sintered profiles

From the AAE values shown in Figure 9, it appears the metamodels are accurately predicting the sintered profiles without the computational expense associated with FEM. The x-

coordinates are well predicted and attain an error of zero at the center of the profile. This is due to the center coordinate being a common x-coordinate for all sintered profiles. Also, the curves are symmetric which is a result of the symmetric nature of the sintering profile. Another aspect to note is that the AAE for the z-coordinate grows as it approaches its maximum value at index 11. This is likely caused by the increased depth of sintering, so the error grows with its magnitude. In order to see this effect more clearly, the Maximum Absolute Error (MAE) values are plotted for the x and z coordinates, respectively in Figure 10.

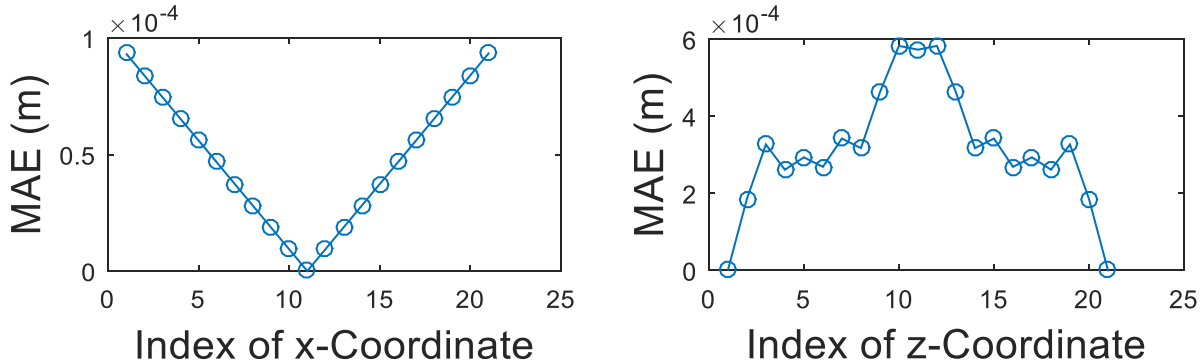

Figure 10. Maximum absolute error of each index for the coordinates of the sintered profiles

It appears again that as z-coordinate increases to its maximum value the maximum error also grows. Surprisingly this maximum error for index 11 is on the same order of magnitude of the z coordinate but this profile associated with this maximum error is an outlier compared to the other profiles used for validation. Because this profile appears to be the only outlier, there is a cautious amount of confidence in the model. For confirmation, the most poorly predicted sintering model as measured by the MAE, and a well-predicted model are shown in Figure 11 along with the true model.

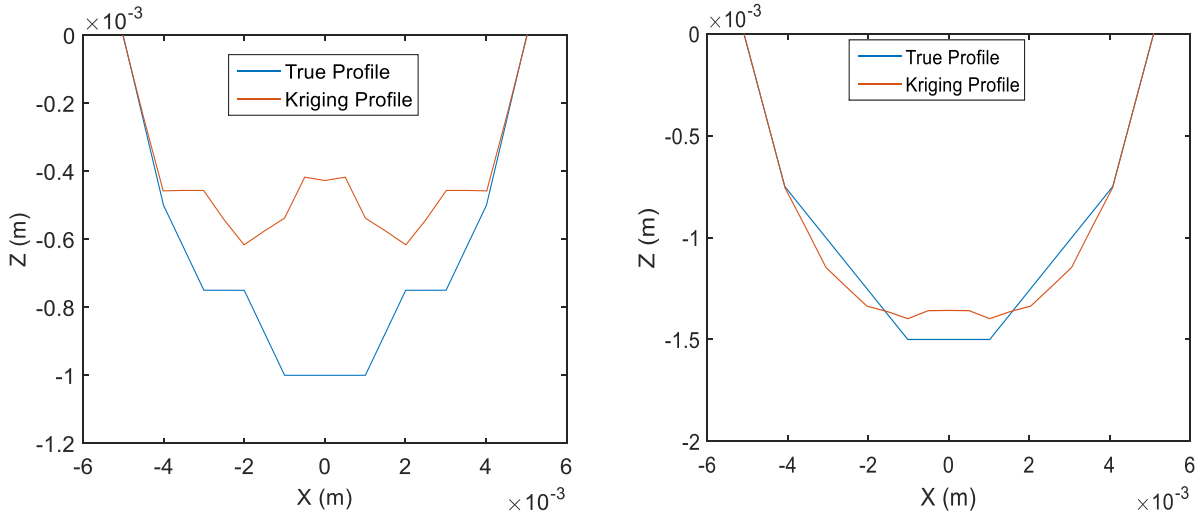

Figure 11. Poorly predicted sintering profile (left) and well predicted sintering profile (right).

From Figure 11, it appears the metamodels struggles with capturing the maximum depth of the sintered profile when compared to the other points of the sintered profile. This is likely because the coordinates associated with the maximum depth have the most variance. Figure 12 shows the variance of each x and z coordinates where it is clear that the z coordinate associated with the maximum depth has the most variance.

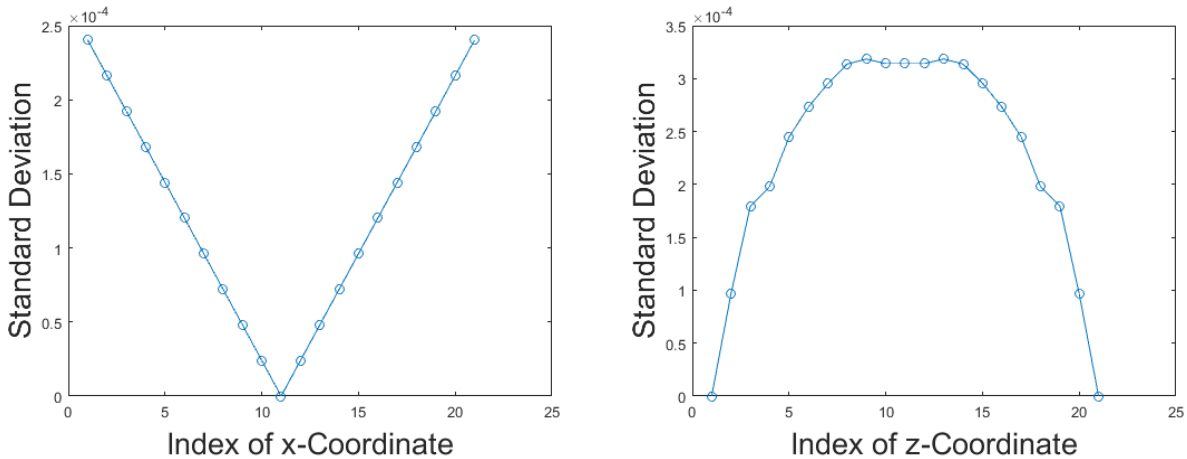

Figure 12. Standard deviation of each index for the coordinates of the sintered profiles

From expert knowledge, it is clear that the center of the sintered profile should be the deepest point of the profile, so an artificial constraint was imposed on the sintered profiles so the maximum depth penetrated was at the center. With this constraint imposed, the agreement between experimental and metamodel is improved, as shown by Figure 13, where the most poorly sintered profile is modified by the constraint.

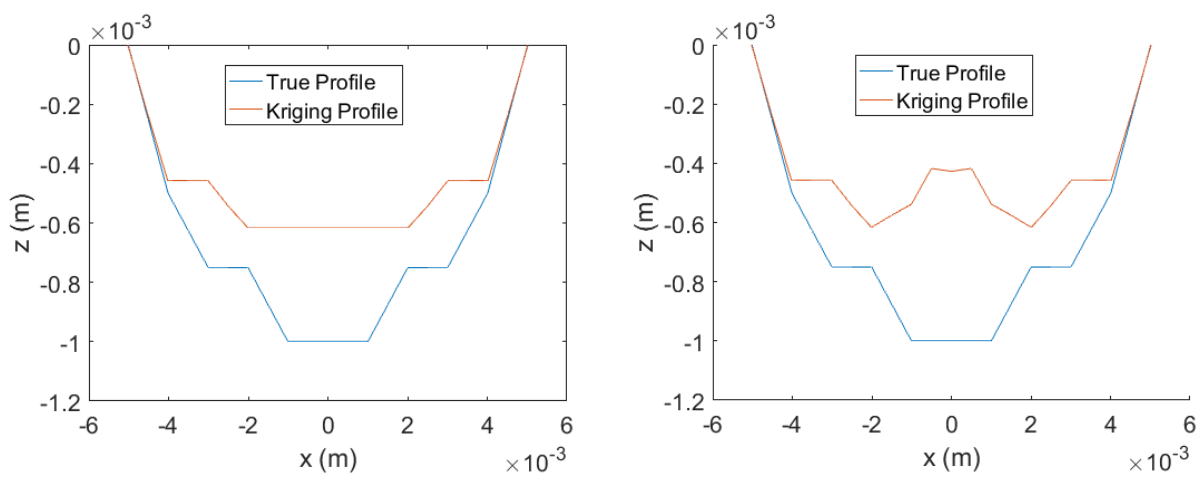

Figure 13. Improvement of predicted sintering profile by imposing maximum depth constraint (left) compared to original Kriging Profile.

Even though the maximum depth has some error, based on the AAE value and visual inspection, the metamodel is effective for predicting the sintered profile. As more data becomes available the model will improve, which will in turn, yield higher performance in the full system model.

Multiobjective Optimization

A complete system model was developed, as previously shown in Figure 1, where the outputs of certain subsystems became the inputs of others. With the full model, the performance space is explored to identify optimal operating parameters. These operating parameters are the values of κ and γ, from Equation 9, as well as the hatch spacing, h. The goal then becomes to determine the operating conditions given a certain weather and location. It is emphasized that the parameters are optimized for a given day since the parameters will vary with weather conditions. In order to determine these optimal operating parameter values, first, the objectives must be defined.

There are three objectives for this problem. The first of which is minimizing the power required to operate the system, p_{RMS} which is an output of the mechatronics model. The second objective is to maximize the quality of the tiles which is quantified by minimizing the volume of sand that is left non-sintered. This quantity is provided from the path planning model and heat transfer metamodel. Finally, the last objective to minimize the manufacturing time is equivalent to minimizing t_{sinter} which is also output by the mechatronics model.

In order to determine the feasible performance of the system a Halton sequence of 5000 points was generated for the three parameters of interest, $\kappa, \gamma,$ and h. The bounds of the parameters are shown in Table 1.

	Parameter	Value
Path Planning	l_{tile}	0.1524 m
	w_{tile}	0.1524 m
Mechatronics	m_{bed}	6 kg
	m_{gantry}	1 kg
	μ	0.5
	r_{gear}	5 mm

	Parameter	Value
Heat Transfer	ρ_{sand}	1515 kg/m^3
	e_{sand}	0.9
	h_{air}	2.0
	T_a	300 K
	K_{sand}	0.27 W/mK
	C_{sand}	800 J/kgK
	T_{melt}	1883 K

Table 1. Various values of the constants used in the solar sintering model.

These design points were then input to the solar sintering model to determine the objective values. Unfortunately not all performances yielded by the model are physically feasible. The first constraint is the time of exposure cannot exceed 20s. This is imposed so the tile will complete in a reasonable amount of time. The second constraint is the depth of the sintered profile must be between 1mm and 1.5mm which is the target depth of sintering. The final constraint is imposed by the motors driving the bed. Figure 14 shows the torque curve of the motor which must be obeyed, so parameters that lead to a violation of this curve are neglected as well.

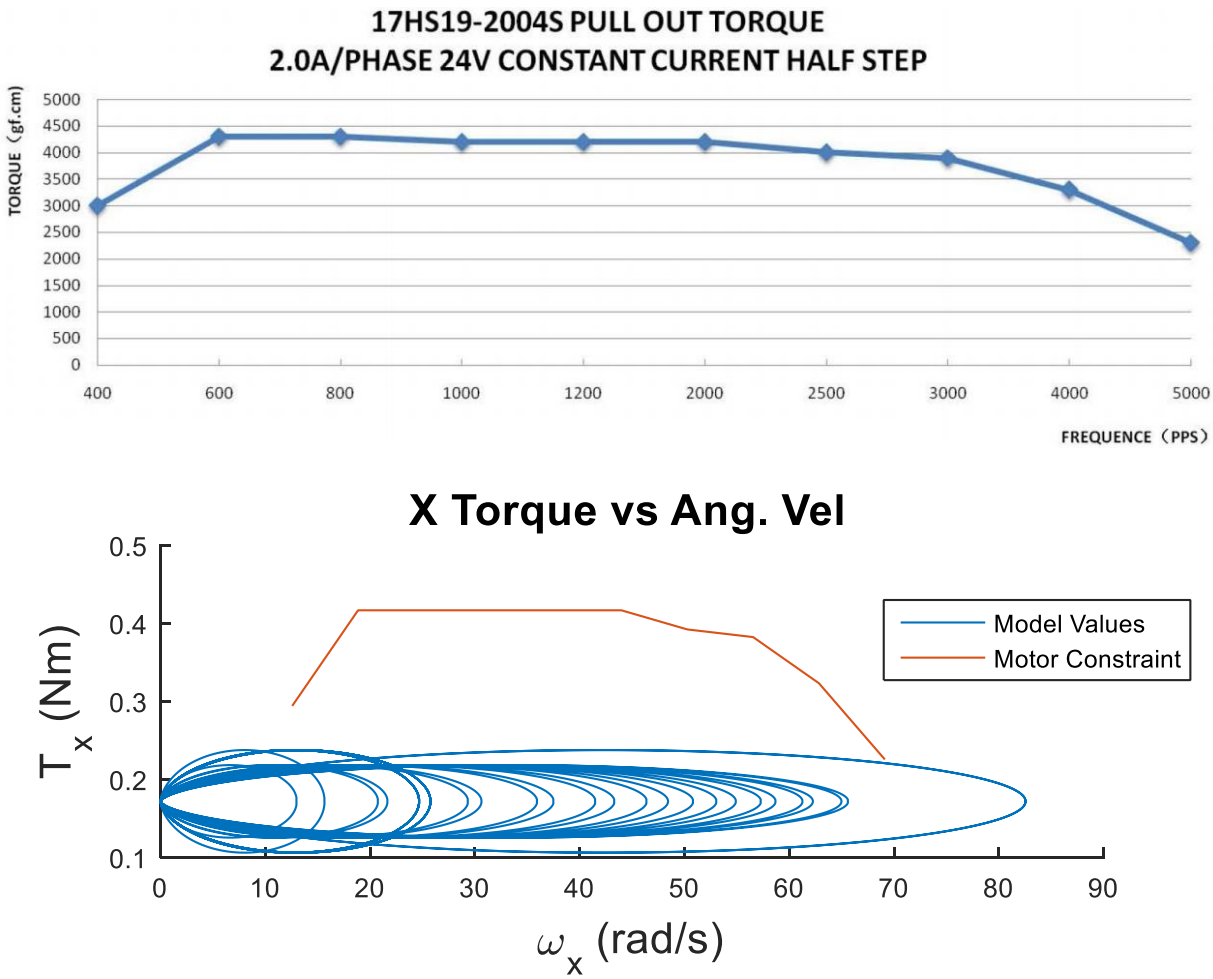

Figure 14. Torque Curve for the motors used which imposes constraints on the motion planning (Top) and an example Torque curve bounded by motor constraints (Bottom)

With the constraints imposed, computation of the performance was completed using the values shown in Table 2.

Parameter	Bounds
κ	[1,700]
γ	[0.1,1]
h	[0.0016,0.01]

Table 2. Bounds of the Halton sequence used to determine the performance space.

With the performance space determined the Pareto frontier was identified to determine optimal performance and parameter values.

Pareto Frontier Identification

Upon inspection it is clear that minimizing p_{RMS} is at opposition to minimizing t_{sinter}, because if the system is running quickly it also will be consuming energy at a faster rate. Due to the opposing nature of the objectives of this problem, it was anticipated that there will not be a single optimal solution, but rather a set of Pareto solutions. In order to identify the Pareto solutions, a non-dominating algorithm was used to identify the Pareto frontier. For the weather conditions and lens angles shown in Table 3, various Pareto Frontier and associated design spaces were generated.

$\frac{I_{in}}{I_{max}}$	Lens Angle (°)
0.7000	24.0
0.6000	18.0
0.7667	12.0
0.6667	6.0
0.5667	28.8
0.7333	22.8
0.6333	16.8
0.5333	10.8
0.7889	4.8
0.6889	27.6

Table 3. Weather conditions and lens angles used to identify Pareto Frontiers

A small sample of the Pareto Fronts and the designs associated with the Pareto Front are displayed in this report for clarity in Figure 15 and Figure 16.

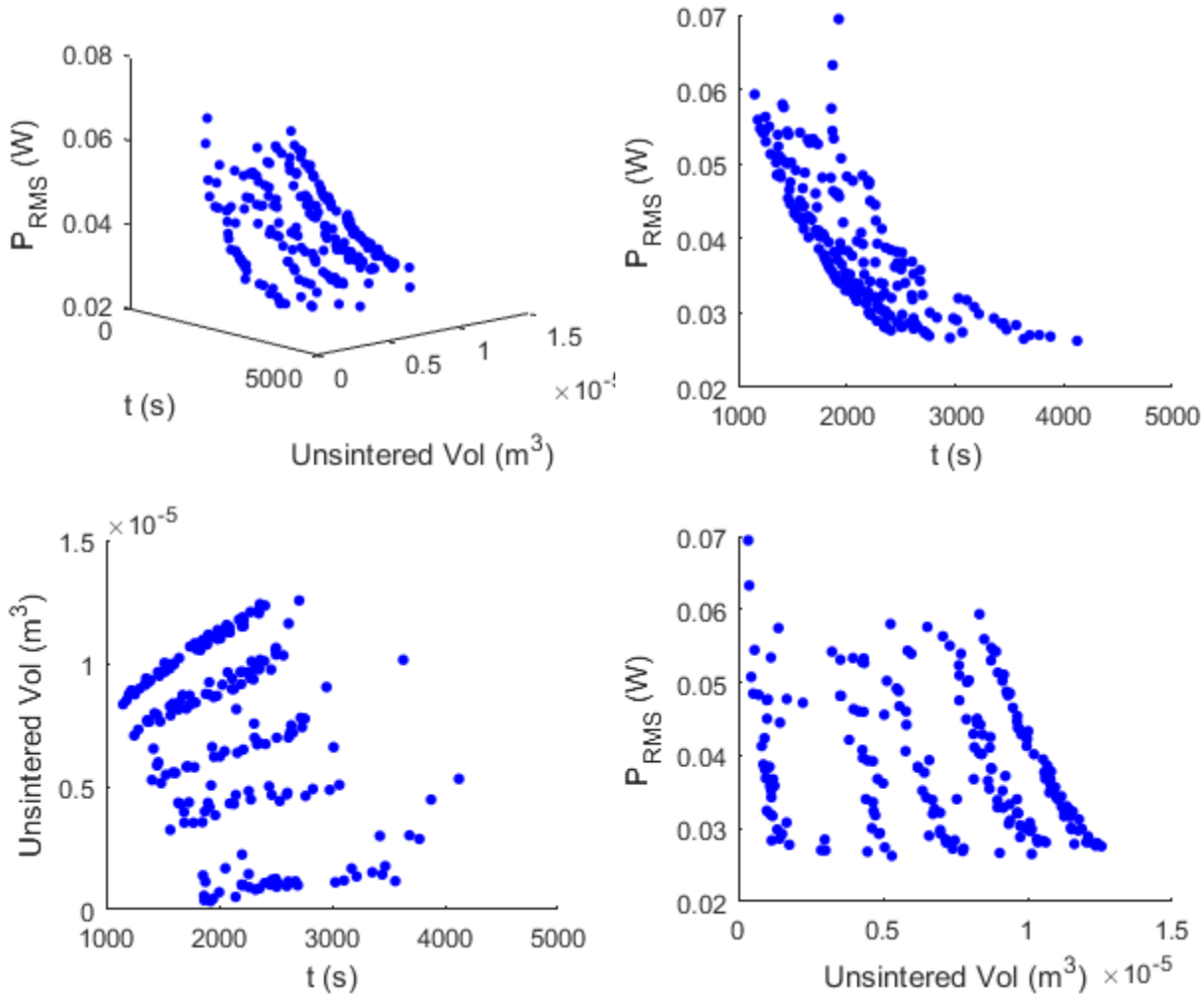

Figure 15. Pareto Frontier of day where $\frac{I_{in}}{I_{max}} = 0.5667$ and lens angle $= 28.8$.

From Figure 15, it can be seen that a clear, generally cconvex Pareto front was identified. The conditions of the day are such that the intensity of the sun is relatively low and the angle of the lens is dramatic. These are worst case operating parameters, because the time needed to produce a layer of the tile will be the longest of any other time. There is a clear minimum amount of time needed to produce a tile. The tradeoff between time and power is very clear in the top right plot where the longer it takes to produce a tile the less power it takes to produce. This behavior exactly matches the predictions made and lends credibility to the model. Somewhat unsurprisingly, there appears to be little dependence of the sintered volume on the other objectives. This is due to the sintered volume being largely dependent of the hatch spacing rather than the exposure time when the depth of penetration is a constraint. The hatch spacing seems to have a small impact on the total time to sinter and power requirements.

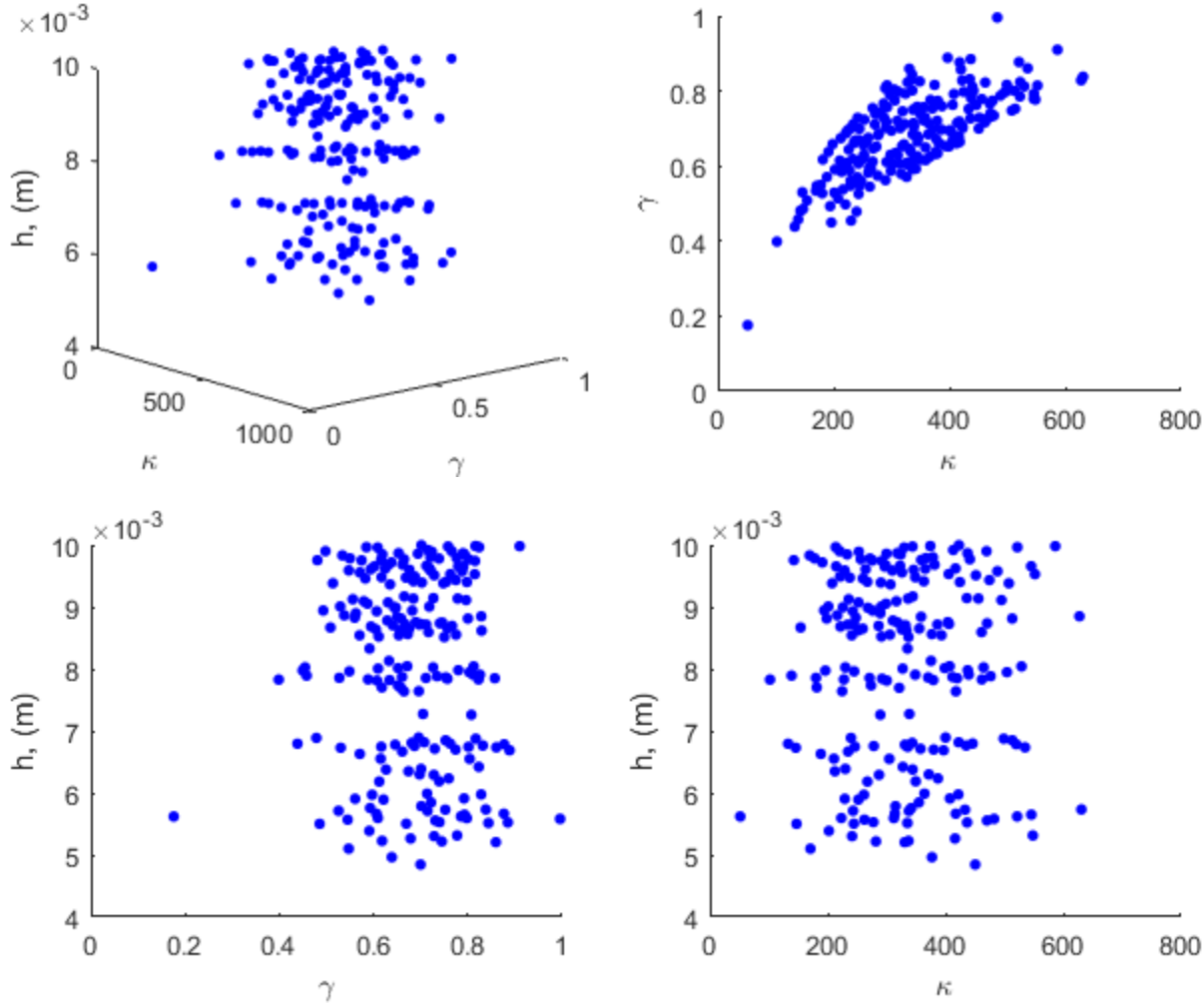

Figure 16. Design Space associated with Pareto Frontier of day where $\frac{I_{in}}{I_{max}} = 0.5667$ and lens angle $= 28.8$.

The design parameters that yield the Pareto front corroborate the results of the performance space. There appears to be little dependence between the road width and motion planning parameters that control the total time to produce a tile and power requirements. There is a dependence between the two motion planning parameters, that is due to the Torque curve constraints. There appears to be a nonlinear relationship between the two motion planning parameters. In order to compare the difference in the parameter space due to weather conditions, a second determination of the Pareto Frontier and design space was performed on a near ideal day where $\frac{I_{in}}{I_{max}} = 0.7889$ and lens angle $= 4.8$ and the results are shown in Figure 17 and Figure 18.

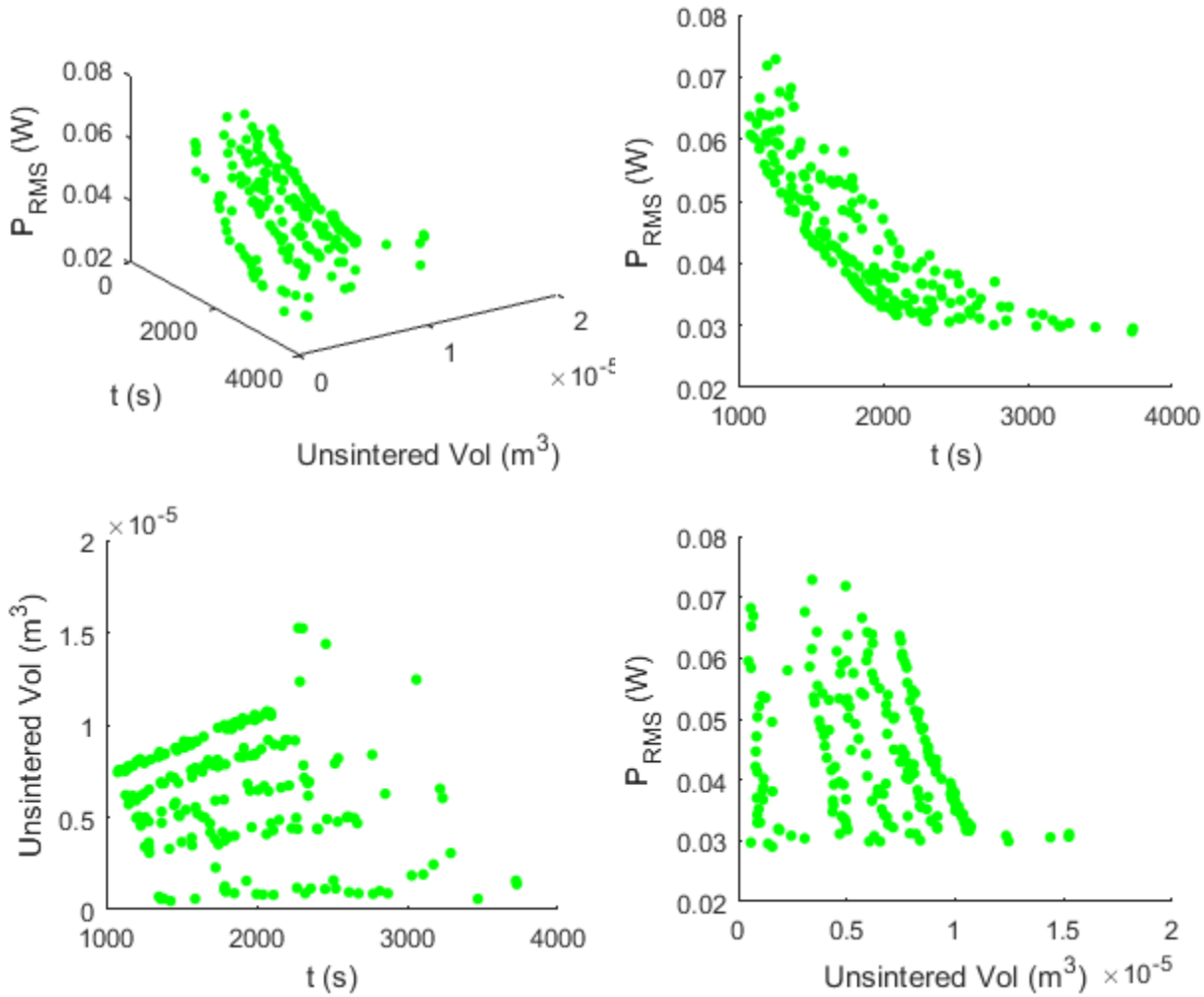

Figure 17. Pareto Frontier of day where $\frac{I_{in}}{I_{max}} = 0.7889$ and lens angle $= 4.8$.

Again from Figure 17 it can be seen that a clear, generally convex Pareto front was identified. The conditions of the day are such that the intensity of the sun is relatively high and the angle of the lens is nearly zero. These are close to the best case operating parameters, because the time needed to produce a layer of the tile will be the shortest of any other time. There is a clear minimum amount of time needed to produce a tile. The tradeoff between time and power is again very clear in the top right plot, where the longer it takes to produce a tile the less power it takes to produce.

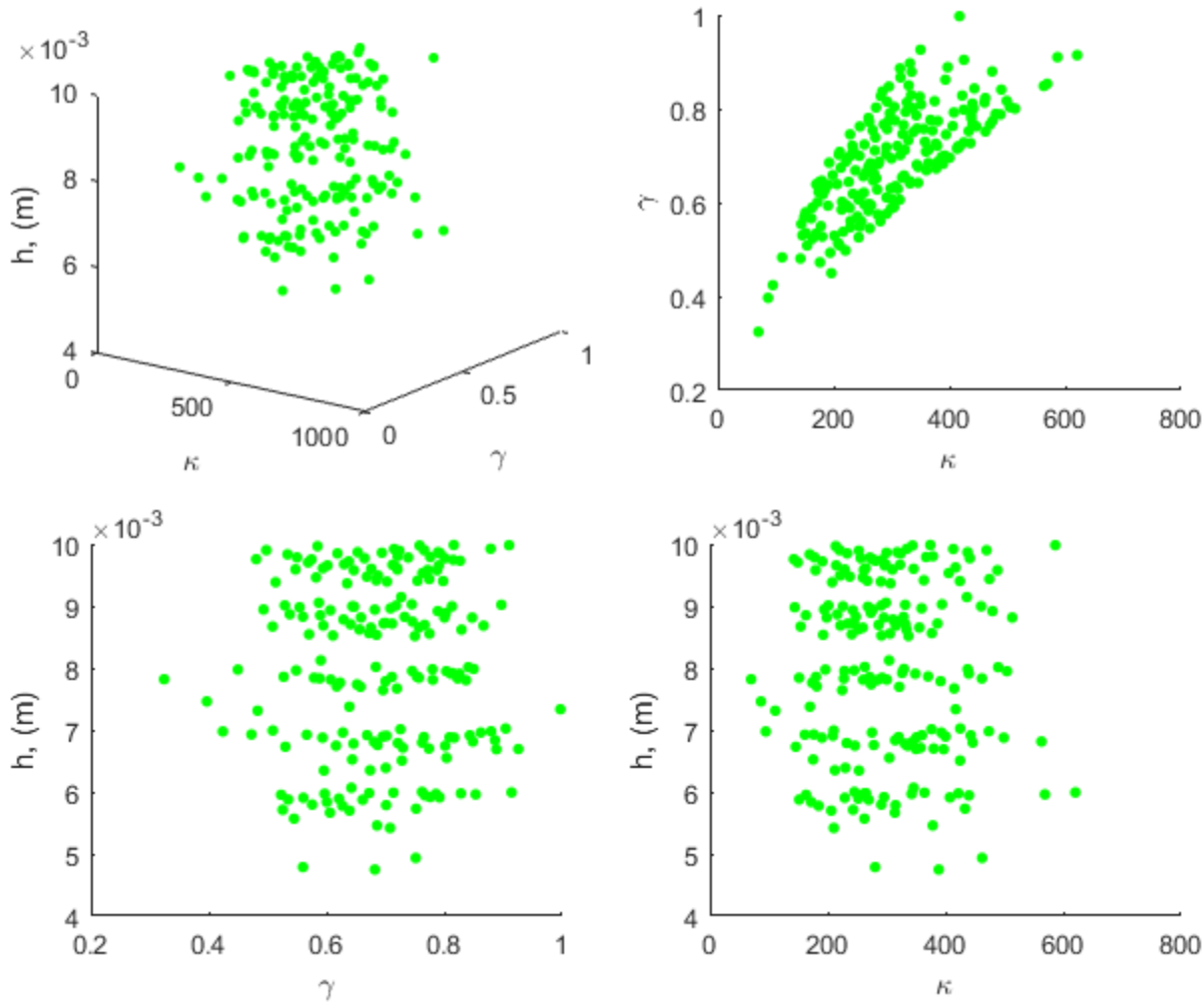

Figure 18. Design Space associated with Pareto Frontier of day where $\frac{I_{in}}{I_{max}} = 0.7889$ and lens angle $= 4.8$.

The design parameters that yield the Pareto front again are very similar to the results of the previous day but in order to see the differences the parameters of the design space as well as the performance space must be plotted simultaneously, as shown in Figure 19.

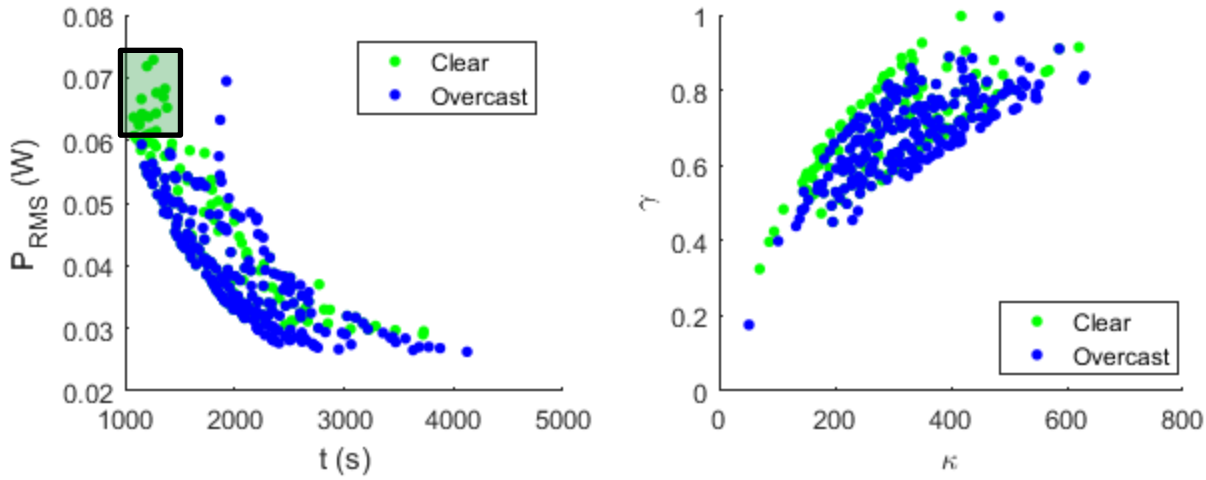

Figure 19. Comparison of the performance and design spaces for an overcast day (orange) and clear day (blue).

Figure 19 yields some very interesting results. While in general, the days have very similar design and performance spaces there are some slight but intuitive differences. As expected, the clear day is able to produce tiles at a faster rate at a higher power requirement when compared to the cloudy day. The green rectangle of the left plot of Figure 19 illustrates this performance region. The design parameters associated with this performance were identified and used to determine the depth of sintering for both the clear and cloudy days. This was done to test the hypothesis that the cloudy day would not obtain the minimum required sintering depth while the clear day would. Figure 20 displays these results where the maximum sintered depth is plotted against the index of the sets of design parameters. For clarity, there were 26 different designs that lead to the green performance region of Figure 19 so there are 26 different sets of design parameters that were evaluated on a clear and cloudy day. The horizontal axis indicates the index of the different sets of design parameters used. Also it can be seen from Figure 19 that for the design parameters that lead to a longer tile production time, the cloudy day is able to operate at a lower power requirement. This is likely because the exposure time can be longer without over sintering the tile. If the motors move too slowly on a sunny day, the tiles will over sinter.

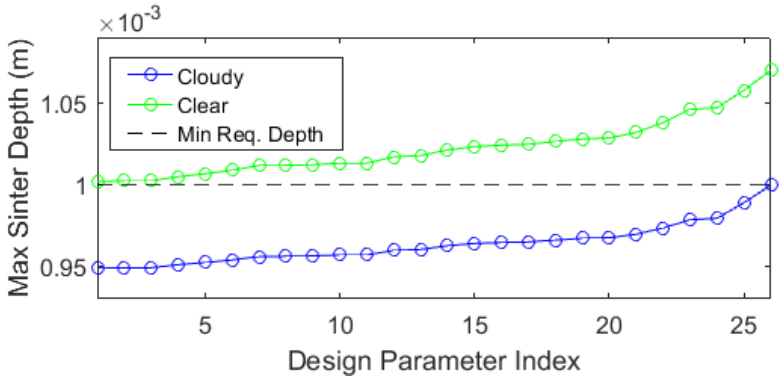

Figure 20: Maximum depth sintered for the set of design parameter of interest for a clear and cloudy day.

As expected, the cloudy day could not sinter to the desired depth because the motors were running to quickly but the clear day was able to obtain the desired depth.

Conclusions

The Solar Sintering Station is a complicated system, in part, due to the large variation in the energy source. Since the sun provides the energy, the amount of energy entering the system depends on when and where the system is operating. Therefore, the Fresnel Lens model has to account for this by computing the solar angle and intensity for many different operating parameters. As explained, the outputs from the Fresnel Lens model, became inputs into the Path Planning, Mechatronics, and Heat Transfer Model. The Path Planning model determined where the sand bed needed to move so the Mechatronics model could determine how to move the sand bed. Once the path was planned and the exposure time was calculated, the Heat Transfer model calculated the sintered depth, and non-sintered region to quantify part quality. Due to the computational expense of the Abaqus simulations, a metamodel was formed for the Heat Transfer model. Finally, all models were put together for the Multiobjective model to search for Pareto Solutions and visualize the objective tradeoffs.

Due to the variation in light intensity focused on the sand bed, there are Pareto Frontiers for each combination of intensity and lens angle. For all tested combinations, there were two large dependencies, power vs. time and κ vs. γ. The competing relationship between power and time was expected since running the motors faster, in general, requires more power. The dependency between κ and γ arises, largely, because of the torque constraint. When comparing a clear day to a cloudy day, the clear day could reach areas of performance and design spaces that could not be achieved on a cloudy day. The main reason being weather causes a variation in intensity from the clouds blocking some of the light. The main takeaway was that the motors should run faster on a clear day and slower on a cloudy day to achieve the correct sintered depth. More investigation into the results is needed to fully understand the Pareto Solutions.

Throughout the project, linking system models along with a metamodel to multiobjective optimization was explored for solution visualization. While system optimization was easy, getting the models to work together was actually quite difficult. The system had several dependencies that caused information flow to become convoluted. Additionally, getting the Path Planning model to correctly fit a hatch pattern for an arbitrary shape was more challenging than expected. With more time, it would have been beneficial to explore different metamodels to see impacts on the results. The main discovery about the system was that the sintered sand cools down too much during the path cycle, such that additional passes do not improve part quality. This discovery was important in optimizing the system.

References

[1] M.-J. Rietema, "Design of a Solar Sand Printer," University of Twente, 2013.

[2] Y. Tang, J. Fuh, H. Loh, Y. Wong and L. Lu, "Direct Laser Sintering of a Silica Sand," *Materials and Desin,* vol. 24, no. 8, pp. 623-629, 2003.

[3] J. e. a. Song, "Rapid prototyping manufacturing of silica sand patterns based on selective laser sintering," *Journal of Materials Processing Technology,* vol. 187, pp. 614-618, 2007.

[4] Earth System Research Laboratory, "Solar Calculation Details," [Online]. Available: https://www.esrl.noaa.gov/gmd/grad/solcalc/calcdetails.html. [Accessed 6 March 2017].

[5] Green Power Science, "61" SPOT FRESNEL LENS FRAMED," [Online]. Available: http://www.greenpowerscience.com/FRESNELSHOP/65INCHSPOT.html. [Accessed 23 March 2017].

[6] M. Kharseh, *Solar Radiation Calculation.*

[7] H. Baig, K. C. Heasman and T. K. Mallick, "Non-uniform Illumination in Concentrating Solar Cells," *Renewable and Sustainable Energy Reviews,* pp. 5890-5909, 2012.

[8] H. T. Eyyuboğlu and M. Bayraktar, "Propagation properties of cylindrical sinc Gaussian beam," *Journal of Modern Optics* , pp. 1706-1712, 2016.

[9] R. Abbas and J. M. Martinez-Val, "Analytic optical design of linear Fresnel collectors with variable widths and shifts of mirrors," *Renewable Energy,* vol. 75, pp. 81-92, 2015.

[10] R. Leutz and et al., "Design of a nonimaging Fresnel lens for solar concentrators," *Solar energy,* vol. 65, no. 6, pp. 379-387, 1999.

[11] T. L. Bergman, S. A. Lavine, F. P. Incropera and D. P. Dewitt, Fundamentals of Heat and Mass Transfer, 7th ed., Hoboken: John Wiley & Sons, Inc., 2011.